Int. J. Electrochem. Sci., 17 **(2022)** Article Number: 221273, doi: 10.20964/2022.12.72

International Journal of
ELECTROCHEMICAL
SCIENCE
www.electrochemsci.org

Solid-State Preparation and Electrochemical Properties of Mg^{2+}-doped $LiFe_{0.7}Mn_{0.3}PO_4/C$ as Cathode Material for Lithium-Ion Batteries

Kai Xia [1], *Rui Liang*[2], *Yi Luo*[1], *Anqiao Zheng*[1], *Guodong Jiang*[1,3], *Mingxia Fan*[1,3], *Jian Xiong*[1,3], *Songdong Yuan*[1,3,*]

[1] Hubei Collaborative Innovation Center for High-efficiency Utilization of Solar Energy, Hubei University of Technology, Wuhan 430068, China
[2] Sunwoda Electronic Co.,Ltd, Shenzhen 518108, China
[3] The Synergistic Innovation Center of Catalysis Materials of Hubei Province, Wuhan 430068, China
[*]E-mail: 171245675@qq.com

Received: 14 October 2022 / *Accepted:* 19 November 2022 / *Published:* 27 December 2022

A series of $LiFe_{0.7}Mn_{0.3-x}Mg_xPO_4/C$ (x = 0, 0.02, 0.05, and 0.08) cathode materials were synthesized by a high-temperature solid-phase method and characterized by X-ray diffraction, scanning electron microscopy, X-ray photoelectron spectroscopy, and electrochemical tests to determine the structural, morphological, and electrochemical properties of the synthesized materials. The experimental results showed that the small amount of Mg^{2+} doping not only had no effect on the crystalline structure of the material but also significantly improved the electrochemical properties of the material. The $LiFe_{0.7}Mn_{0.25}Mg_{0.05}PO_4/C$ material achieved specific discharge capacities of 163.2, 155.2, 149.1, and 142.0 mAh/g at 0.1C, 0.2C, 0.5C, and 1C, respectively, and a capacity retention rate of 98.6% after 50 cycles at 0.1C. It exhibited excellent rate performances and cycling stability. Electrochemical alternating-current impedance showed that the lithium-ion diffusion coefficient of the $LiFe_{0.7}Mn_{0.25}Mg_{0.05}PO_4/C$ sample reached 1.19×10^{-13} cm^2/s, which was 4.1 times higher than that of the pre-modified sample. Combined with the cyclic voltammetry test results, it was found that the appropriate amount of Mg^{2+} doping could reduce the impedance and polarization of the material as well as increase the conductivity and the lithium-ion diffusion rate, ultimately improving the electrochemical properties.

Keywords: lithium-ion battery, $LiFe_{0.7}Mn_{0.3}PO_4$, ion doping, electrochemical performance

1. INTRODUCTION

As a cathode material for lithium-ion batteries, lithium iron phosphate ($LiFePO_4$) has attracted widespread attention due to its high theoretical capacity (170 mAh/g), moderate operating voltage (3.5 V vs. Li^+/Li), environmental friendliness, low cost, and good safety characteristics [1–3]. However, the

inherent low electronic conductivity (10^{-9}–10^{-10} S cm^{-1}) and ionic conductivity (10^{-14}–10^{-15} S cm^{-2}) of $LiFePO_4$ itself leads to its poor power performance and therefore poor cycling and multiplier performance when it is used as a power cell material. Many researchers have worked on optimizing the modification of $LiFePO_4$ to obtain better electrochemical properties, such as carbon or metal oxide cladding [4, 5], doping with transition metal ions [6, 7], and preparing nanoscale particles of the material [8, 9].

Compared to $LiFePO_4$, $LiMnPO_4$ has a higher operating voltage (4.1 V vs. Li^+/Li), and its theoretical energy density is 111 Wh/kg higher than that of $LiFePO_4$ (586 Wh/kg). Thus, it exhibits a higher energy density. In addition, $LiMnPO_4$ has better electrolyte adaptability with commercial oxide cathode materials [10, 11]. However, $LiMnPO_4$ has a much lower electronic conductivity (<10^{-10} S cm^{-1}) and ionic conductivity (10^{-14}–10^{-17} S cm^{-2}) and undergoes the John–Teller effect, leading to lattice deformation and structural changes. As a result, the actual specific capacity of $LiMnPO_4$ is much lower than the theoretical value [12, 13]. However, similar to $LiFePO_4$, $LiMnPO_4$ can be modified by carbon cladding [14, 15], ion doping [16, 17], or reducing the material size [18, 19] to improve its electrochemical properties.

To overcome the limitations of single-transition metal phosphates, solid solution $LiFe_xMn_{1-x}PO_4$, which also has an olivine structure, has been extensively investigated [20, 21]. This is because the Mn^{2+} radius is larger than that of Fe^{2+}, so Mn substitution of some of the Fe sites can widen the Li^+ diffusion channels and increase the diffusion rate of Li^+. Thus, $LiFe_xMn_{1-x}PO_4$ has better electrochemical properties than single $LiFePO_4$ or $LiMnPO_4$ [22, 23]. Many studies have shown that for the $LiFe_xMn_{1-x}PO_4$ system formed by Mn^{2+}-doped $LiFePO_4$, the capacity of the material decreases to some extent with increasing Mn^{2+} doping content. This is caused by excess Mn^{2+} doping, resulting in a decrease in the electronic conductivity of the material. Therefore, a small amount of Mn^{2+} doping can both reduce the capacity loss and improve the electronic conductivity of the material, and it can serve to balance the two. Liu et al. [24] prepared a series of $LiFe_{1-x}Mn_xPO_4/C$ ($0 \le x \le 0.8$) materials by a solid-phase method. It was found that $LiFe_{0.8}Mn_{0.2}PO_4/C$ had a first specific discharge capacity of up to 150 mAh/g at 0.1C and a retention rate of 97.6% after 50 cycles, which was higher than those of samples with other Mn-doping ratios. This suggests that a small amount of Mn^{2+} doping into $LiFePO_4/C$ can improve its electrochemical performance, likely because a moderate amount of Mn can effectively improve the kinetic diffusion of Li^+ and form super exchange interactions between Fe-O-Mn ions.

However, $LiFe_xMn_{1-x}PO_4$ still inevitably suffers from low electronic conductivity and ionic conductivity, and many researchers have proposed carbon capping or particle size reduction, but both of these methods reduce the energy density of the material, thus limiting the commercial progress of the material [25]. Therefore, doping with transition metal ions is the best way to modify $LiFe_xMn_{1-x}PO_4$, which can simultaneously stabilize the structure and improve the electrical conductivity of the material. Gao et al. [26] prepared $Li(Fe_{0.6}Mn_{0.4})_{0.96}Ti_{0.02}PO_4/C$, which exhibited excellent performances. The results showed that Ti^{4+} doping did not change the crystal structure of the target material but improved the discharge performance of the material at high magnification, reaching discharge capacities of 134.7 and 124.4 mAh/g at 10C and 20C, respectively, because the Ti^{4+} doping resulted in a reduction of the electrochemical impedance and polarization of the material. Xiao et al. [27] successfully synthesized $LiFe_{0.4}Mn_{0.6-x}Cr_xPO_4/C$ ($x \le 0.01$) with different amounts of Cr^{3+} doping by the solid-phase ball milling

method. Among the synthesized samples, $LiFe_{0.4}Mn_{0.595}Cr_{0.005}PO_4/C$ had the highest specific discharge capacity, excellent multiplicative performance and cycling retention, with discharge capacities of 164.0 and 147.5 mAh/g at 0.1C and 2C, respectively, and retention rates as high as 99.2% after 50 cycles at 0.1C. The retention rate after 50 cycles at 0.1C was 99.2%. In addition, the electronic conductivity and ionic diffusion coefficient of $LiFe_{0.4}Mn_{0.595}Cr_{0.005}PO_4/C$ were increased by factors of 5.3 and 6.4, respectively, compared to those of the undoped Cr sample. These results indicated that ion doping modified the electrochemical properties of the material significantly.

Considering that there are few studies on $LiFe_{0.7}Mn_{0.3}PO_4$, the present work successfully prepared $LiFe_{0.7}Mn_{0.3-x}Mg_xPO_4/C$ (x = 0, 0.02, 0.05, and 0.08) by a high-temperature solid-phase method and explored the effect of Mg^{2+} doping on its electrochemical properties. The results showed that $LiFe_{0.7}Mn_{0.25}Mg_{0.05}PO_4$ exhibited excellent rate performances. The specific discharge capacity at 1C reached 142.0 mAh/g and had good cycling stability.

2. EXPERIMENTAL

2.1. Materials

The LiH_2PO_4, $FeC_2O_4{\cdot}2H_2O$, $MnC_4H_6O_4{\cdot}4H_2O$, and $MgC_4H_6O_4{\cdot}4H_2O$ were of analytical grade and were purchased from Aladdin Biochemical Technology Co., Ltd. (Shanghai, China). These reagents were used as received.

2.2. Preparation of $LiFe_{0.7}Mn_{0.3-x}Mg_xPO_4/C$ (x = 0, 0.02, 0.05, and 0.08)

LiH_2PO_4, $FeC_2O_4{\cdot}2H_2O$, $MnC_4H_6O_4{\cdot}4H_2O$, and $MgC_4H_6O_4{\cdot}4H_2O$ in certain molar ratios were weighed as raw materials. Sucrose and ascorbic acid were used as the carbon source and reducing agent, respectively, and they were mixed with anhydrous ethanol in specified amounts. The material was then separated from the ethanol and dried overnight at 60°C in a vacuum oven. The target material $LiFe_{0.7}Mn_{0.3-x}Mg_xPO_4/C$ (x = 0, 0.02, 0.05, and 0.08) was obtained by pre-combustion at 350°C for 4 h in an argon atmosphere at a rate of 5°C/min and then calcined at 650°C for 12 h. The carbon content of the target material was about 3 wt%.

2.3. Characterization

The crystal structures of the samples were analyzed using an Empyream X-ray diffractometer from Panacol (The Netherlands), and the cell parameters were refined using the JADE software. The surface morphologies of the electrode materials were observed via scanning electron microscopy (SEM, Zeiss Gemini 330), and the elemental distributions were analyzed using an accompanying energy-dispersive X-ray spectroscopy (EDS) system. The surface compositions of the samples were analyzed by X-ray photoelectron spectroscopy (XPS, Thermo Fisher K-Alpha+).

2.4. Electrochemical measurements

The positive electrode sheets were weighed according to the mass ratio of $LiFe_{0.7}Mn_{0.3-x}Mg_xPO_4$/C: conductive carbon black: polyvinylidene fluoride (PVDF) = 8:1:1. They were mixed with N-methyl pyrrolidone (NMP) to form a paste evenly that was coated on aluminum foil, dried completely at 100°C overnight, and then rolled into 12-mm-diameter electrode discs after forming. CR2032-type button cells were assembled in an argon atmosphere glove box with lithium metal sheets as the negative electrode, porous polyethylene films as the septum, and 1 mol/L $LiPF_6$ (ethylene carbonate (EC): dimethyl carbonate (DMC): methyl ethyl carbonate (EMC) = 1:1:1) as the electrolyte.

The battery test system was a LAND CT2001 (Wuhan, Hubei), with a constant current and voltage charge/discharge voltage range of 2.0–4.5 V. Cyclic voltammetry tests were carried out on an electrochemical workstation CHI660D (Huachen, Shanghai) with a scan rate of 0.1 mV/s and a scan range of 2.0–4.5 V. Alternating-current (AC) electrochemical impedance spectroscopy (EIS) was performed on the electrochemical workstation between 10 mHz and 100 kHz with an amplitude of 5 mV.

3. RESULTS AND DISCUSSION

Fig. 1 shows the XRD patterns of the $LiFe_{0.7}Mn_{0.3-x}Mg_xPO_4$/C samples. It can be seen that the diffraction peaks of all the samples corresponded to the lithium iron phosphate standard PDF# 40-1499 card, indicating that the products had a single-phase olivine-type structure and belonged to the orthogonal crystal system (Pmnb space group) [28]. No significant impurity peaks appeared in the pattern, indicating that Mg^{2+} doping did not affect the crystalline structure of the $LiFe_{0.7}Mn_{0.3-x}Mg_xPO_4$. In addition, the main diffraction peaks were strong and narrow, indicating good crystallinity of the prepared samples. No diffraction peaks were observed in the XRD spectra corresponding to the surface-covered carbon of the material, which could be the result of amorphous carbon or too small of a carbon content after the pyrolysis of sucrose.

In order to obtain more detailed information on the structures of the prepared materials, the resulting XRD patterns were subjected to Rietveld refinement to obtain the values of the cell parameters of the $LiFe_{0.7}Mn_{0.3}PO_4$/C samples with different levels of Mg^{2+} doping. Table 1 shows the values of the cell parameters for the $LiFe_{0.7}Mn_{0.3-x}Mg_xPO_4$/C samples. After Mg^{2+} doping, the cell shrank to some extent along the a, b, and c axes, and the cell volume decreased, as the Mg^{2+} radius was smaller than those of the Fe^{2+} and Mn^{2+}, which is in good agreement with the previously reported data[29,30]. This indicated that the Mg^{2+} doping did not destroy the $LiFe_{0.7}Mn_{0.3}PO_4$/C crystal structure but formed a good $LiFe_{0.7}Mn_{0.3-x}Mg_xPO_4$ solid solution with it. According to the ion doping theory of Chung et al. [31], Mg^{2+} doped into the M1(Li) or M2(Fe/Mn) sites of the $LiFe_{0.7}Mn_{0.3}PO_4$/C tended to occupy the Fe-Mn elemental sites, as Mg^{2+} (r = 0.072 nm) has a smaller ionic radius than Mn^{2+} (r = 0.083 nm) and Fe^{2+} (r = 0.078 nm). Hence, the cell parameters of the $LiFe_{0.7}Mn_{0.3-x}Mg_xPO_4$/C samples progressively decreased.

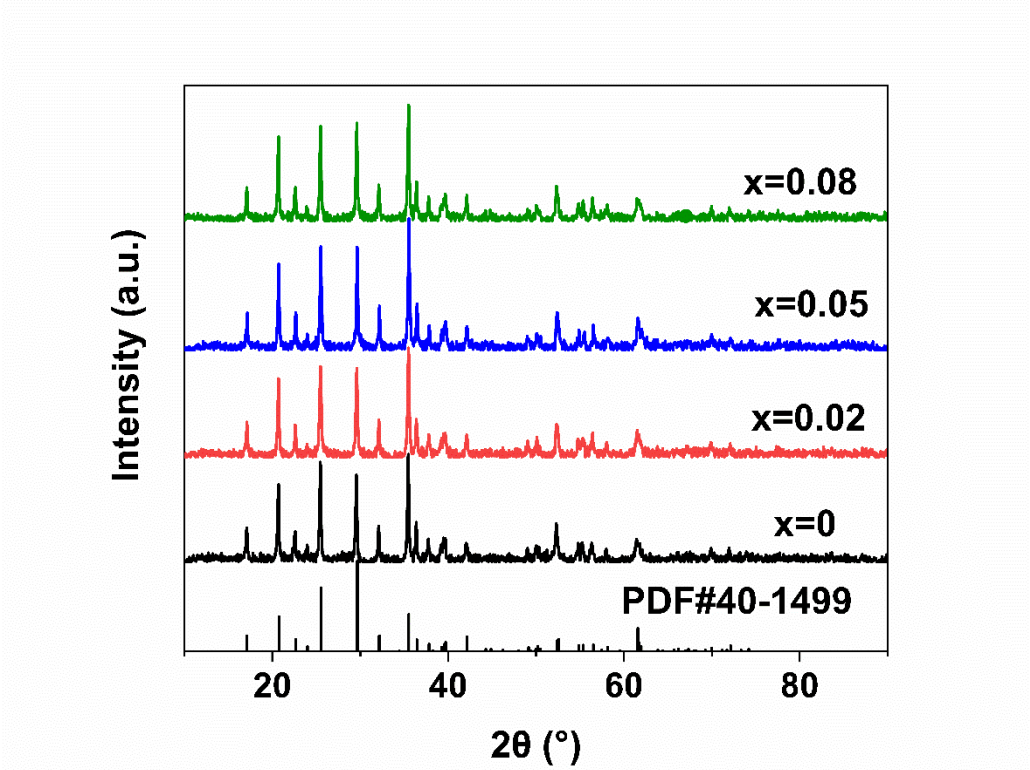

Figure 1. X-ray diffraction (XRD) patterns of $LiFe_{0.7}Mn_{0.3-x}Mg_xPO_4/C$ (x = 0, 0.02, 0.05, and 0.08) composites.

Table 1 Calculated crystal cell parameters of $LiFe_{0.7}Mn_{0.3-x}Mg_xPO_4/C$ (x = 0, 0.02, 0.05, and 0.08) samples.

x	a (Å)	b (Å)	c (Å)	V (Å^3)
0	0.6039	1.0359	0.4712	0.2948
0.02	0.6034	1.0343	0.4710	0.2939
0.05	0.6023	1.0335	0.4705	0.2929
0.08	0.6023	1.0323	0.4706	0.2926

In order to study the morphologies and elemental distributions of the prepared samples, Figs. 2(a) and (b) show the SEM images of the $LiFe_{0.7}Mn_{0.3}PO_4/C$ and $LiFe_{0.7}Mn_{0.25}Mg_{0.05}PO_4/C$, respectively. The particle size distributions of both samples were relatively homogeneous, with these particles ranging in size from 200 to 800 nm and with only a small fraction of tiny agglomerates forming. Compared to the particles of $LiFe_{0.7}Mn_{0.3}PO_4/C$ shown in Fig. 2(a), the particles of $LiFe_{0.7}Mn_{0.25}Mg_{0.05}PO_4/C$ were more uniformly dispersed, and there was a significantly higher proportion of sphere-like particles. This indicated that the doping of Mg could reduce the sizes of the particles to a certain extent, and the sphere-like material with smaller particles was conducive to shortening the diffusion distance of Li^+ and enhancing its electrochemical properties [27]. To further analyze the microscopic morphology of the above $LiFe_{0.7}Mn_{0.25}Mg_{0.05}PO_4/C$ material, TEM images of the complex are shown in Figs. 2(c) and (d). The combination of the two showed that some of the particles appeared to be sphere like, which was consistent with the SEM results. The encapsulated carbon

layer of the $LiFe_{0.7}Mn_{0.25}Mg_{0.05}PO_4/C$ was relatively homogeneous, with a thickness of around 4.0 nm. The homogeneous indeterminate carbon layer not only inhibited the overgrowth of the material but also formed an interconnected conductive network, which significantly increased the electrical conductivity of the material and achieved improvements. The aim was to improve the electrochemical properties of the material. Regular lattice stripes with a lattice width of approximately 0.36 nm, corresponding to the (011) crystal plane, were also clearly observed, indicating that the formation of the material particles was a highly crystalline process. In addition, the compaction densities of the $LiFe_{0.7}Mn_{0.3}PO_4/C$ and $LiFe_{0.7}Mn_{0.25}Mg_{0.05}PO_4/C$ were measured to be 1.666 and 1.683 g/cm^3, respectively, which are higher than those of some of the materials prepared by other researchers shown in Table 2. This showed that the Mg doping facilitated the increase in the compaction density of the material, but the material was still somewhat different from similar materials that are already commercially available.

Table2 Comparison of the compaction densities of materials prepared in other studies and the $LiFe_{0.7}Mn_{0.25}Mg_{0.05}PO_4/C$ material prepared in this study

Material	**Compaction Densitiy(g/cm^3)**	**Reference**
$LiFe_{0.8}Mn_{0.2}PO_4/C$	1.4 g/cm^3	[32]
$LiFe_{0.5}Mn_{0.5}PO_4/C$	1.27 g/cm^3	[33]
$LiFe_{0.48}Mn_{0.48}Mg_{0.04}PO_4$	1.3 g/cm^3	[34]
$LiFePO_4/C$	1.57 g/cm^3	[35]
$LiFe_{0.7}Mn_{0.25}Mg_{0.05}PO_4/C$	1.683 g/cm^3	This work

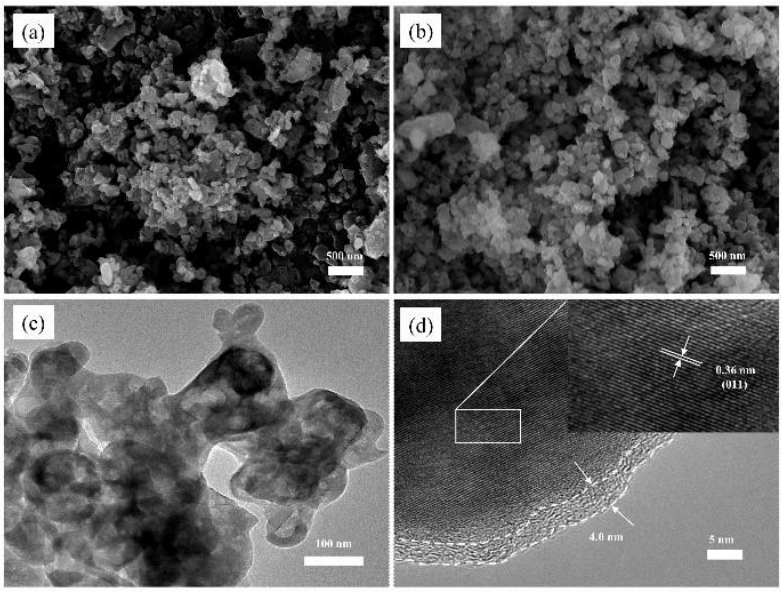

Figure 2. (a) Scanning electron microscopy (SEM) image of $LiFe_{0.7}Mn_{0.3}PO_4/C$. (b) SEM and (c, d) transmission electron microscopy (TEM) images of $LiFe_{0.7}Mn_{0.25}Mg_{0.05}PO_4/C$.

EDS analysis of the $LiFe_{0.7}Mn_{0.25}Mg_{0.05}PO_4/C$ composite was also carried out and the results are displayed in Fig. 3. Fig. 3(a) shows the full EDS spectrum of the material, and typical peaks corresponding to the elements P, O, Fe, Mn, Mg, and C can be clearly seen, which indicates that Mg was

successfully incorporated into the sample. The higher intensity of the Fe peak and the lower intensities of the Mn and Mg peaks were consistent with their high proportions in the chemical composition of the sample. Figs. 3(b)–(h) show the elemental distributions of the composite, with P, O, Fe, Mn, Mg, and C evenly distributed in the material, which further supported the fact that Mg^{2+} was evenly doped in the material. In addition, a uniform distribution of carbon on the surface of this sample was observed.

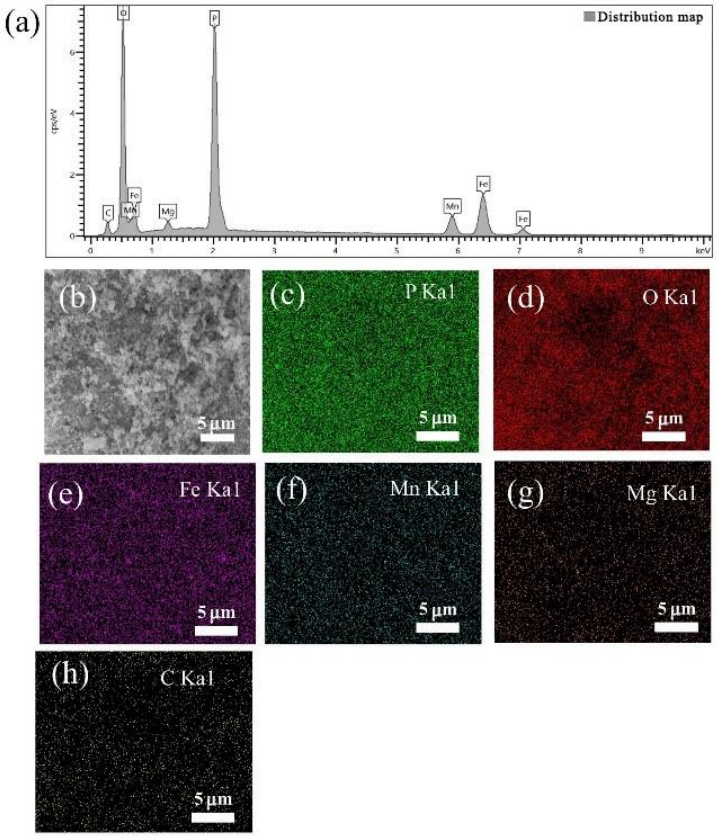

Figure 3. Energy-dispersive X-ray spectroscopy (EDS) elemental distribution maps of $LiFe_{0.7}Mn_{0.25}Mg_{0.05}PO_4/C$ (P, O, Fe, Mn, Mg, and C).

To further investigate the chemical compositions of the samples, XPS tests were used to characterize the valence states of the metal elements, and the fitted results are shown in Fig. 4. Fig. 4(a) shows the full XPS spectrum of the $LiFe_{0.7}Mn_{0.25}Mg_{0.05}PO_4/C$ sample, from which the presence of peaks corresponding to Li 1s, P 2p, C 1s, O 1s, Mn 2p, and Fe 2p can be clearly seen. The Fe 2p spectrum in Fig. 4(b) was split into two peaks at 710.3 and 723.7 eV, corresponding to the Fe $2p_{3/2}$ and Fe $2p_{1/2}$ electron orbital energy levels, respectively, with a binding energy difference of 13.4 eV, indicating that the Fe corresponding to the two peaks was Fe (II). In addition, the electron binding energy had two weak peaks at 714.6 and 727.9 eV corresponding to the Fe $2p_{3/2}$ and Fe $2p_{1/2}$ electron orbital energy levels, respectively. These corresponded to Fe (III), indicating that weak surface oxidation of the material may have partially occurred during the preparation process [36]. In Fig. 3(c), the Mn 2p peak was split into three peaks at 641.0 ($Mn2p_{3/2}$), 642.3 ($Mn2p_{3/2}$), and 653.6 eV ($Mn2p_{1/2}$), corresponding to Mn (II), and a faint peak at 646.4 eV, corresponding to Mn (III), suggesting that some of the Mn was also weakly

oxidized in this material [37]. The Mg 1s peak profile is given in Fig. 3(d) and it was found that the electron binding energy of Mg 1s at 1303.8 eV coincided with the characteristic peak of Mg^{2+}, indicating that the target sample was indeed doped with Mg, which was consistent with the EDS test results.

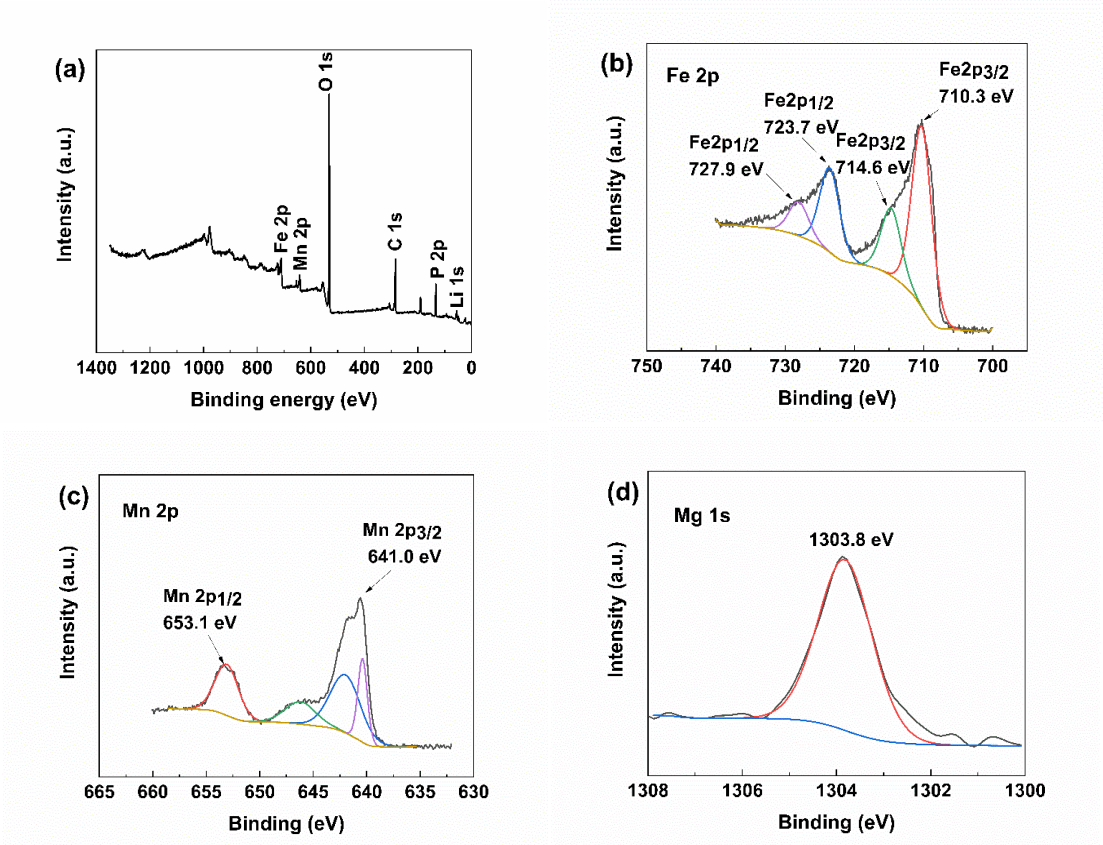

Figure 4. X-ray photoelectron spectroscopy (XPS) spectra of $LiFe_{0.7}Mn_{0.25}Mg_{0.05}PO_4/C$: (a) full survey, (b) Fe 2p, (c) Mn 2p, and (d) Mg 1s spectra.

The electrochemical properties of the $LiFe_{0.7}Mn_{0.3-x}Mg_xPO_4/C$ samples were tested in the charge/discharge voltage range of 2.0–4.5 V. Fig. 5(a) shows the first charge/discharge curves for all samples at 0.1C. It can be seen that all samples had two charge/discharge plateaus corresponding to the Mn^{3+}/Mn^{2+} (4.1 V vs. Li^+/Li) and Fe^{3+}/Fe^{2+} (3.5 V vs. Li^+/Li) redox pairs, which is consistent with the previous researches[38]. The graph also shows that the specific discharge capacity increased from 157.7 to 163.2 mAh/g as the Mg^{2+} doping increased from 0% to 5%, but then decreased to 154.9 mAh/g as the Mg^{2+} doping continued to increase to 8%, indicating that the material had good electrochemical properties when the Mg^{2+} doping was 5%. Fig. 5(b) shows the cycling performance of the $LiFe_{0.7}Mn_{0.3-x}Mg_xPO_4/C$ sample at 0.1C. It can be found that after 50 cycles, the reversible specific capacities of the samples with x = 0, 0.02, 0.05, and 0.08 were 153.1, 155.5, 162.7, and 150.1 mAh/g, respectively, which showed that the $LiFe_{0.7}Mn_{0.25}Mg_{0.05}PO_4/C$ had a higher reversible specific capacity than the other samples. After 50 cycles, a simple calculation revealed that the $LiFe_{0.7}Mn_{0.25}Mg_{0.05}PO_4/C$ sample had a capacity retention rate of 98.6%, which was higher than those of the other samples. Thus, this sample exhibited excellent charge/discharge performances and cycling stability. This was likely because the appropriate amount of Mg^{2+} doping into the $LiFe_{0.7}Mn_{0.3}PO_4/C$ lattice replaced some of the

Mn sites, which reduced the adverse effects of the Jahn–Teller effect and weakened the hindrance of Mn^{3+} on the Li^+ diffusion. However, Mg^{2+} doping increased the intrinsic conductivity of the material, which ultimately improved the cycling performance of the material. Fig. 5(c) shows the performance of the sample at 0.1C, 0.2C, 0.5C, and 1C for five cycles each, and finally back to 0.1C. It can be seen from the graphs that the $LiFe_{0.7}Mn_{0.25}Mg_{0.05}PO_4/C$ sample had the relatively highest specific discharge capacity at any of the multipliers, specifically 149.1 mAh/g at 0.5C and 142.0 mAh/g at 1C. These corresponded to increases of 4.8% and 5.1%, respectively, compared to $LiFe_{0.7}Mn_{0.3}PO_4/C$%. From these results, it can be found that $LiFe_{0.7}Mn_{0.25}Mg_{0.05}PO_4/C$ exhibited a significantly better multiplicative performance than the $LiFe_{0.7}Mn_{0.3}PO_4/C$. This may have been due to the doping of Mg^{2+} into the $LiFe_{0.7}Mn_{0.3}PO_4/C$ lattice to form a solid solution, which increased the disorder of the lattice and thus triggered defects so that the charge in the material lattice was redistributed, and cationic vacancies induced the formation of conductive clusters in the adjacent Mn-O and Fe-O, ultimately increasing the electrical conductivity of the material [39]. In addition, the specific discharge capacity of $LiFe_{0.7}Mn_{0.25}Mg_{0.05}PO_4/C$ in this study was 163.2 mAh/g at 0.1C. By comparing these data with the specific discharge capacities of materials prepared by other researchers shown in Table 3, it can be seen that the $LiFe_{0.7}Mn_{0.25}Mg_{0.05}PO_4/C$ had a higher specific discharge capacity at 0.1C. This was likely due to the relatively small radius of Mg^{2+}, which could effectively reduce the lattice volume change caused by Li^+ during the de-embedding process, which decreased the lattice mismatch near the phase boundary and thus improved the reaction kinetics and rate capability of the electrode [40]. Initially, with the gradual increase in the Mg^{2+} content, this effect became stronger, so $LiFe_{0.7}Mn_{0.25}Mg_{0.05}PO_4/C$ showed good electrochemical stability. However, with the further increase in the Mg^{2+} doping content to 8%, the relative content of electrochemically active material Fe/Mn decreased accordingly, resulting in an increase in the amount of Li^+ that could not be de-embedded from the product lattice, blocking the Li^+ diffusion channels and deteriorating the electrochemical properties of the material.

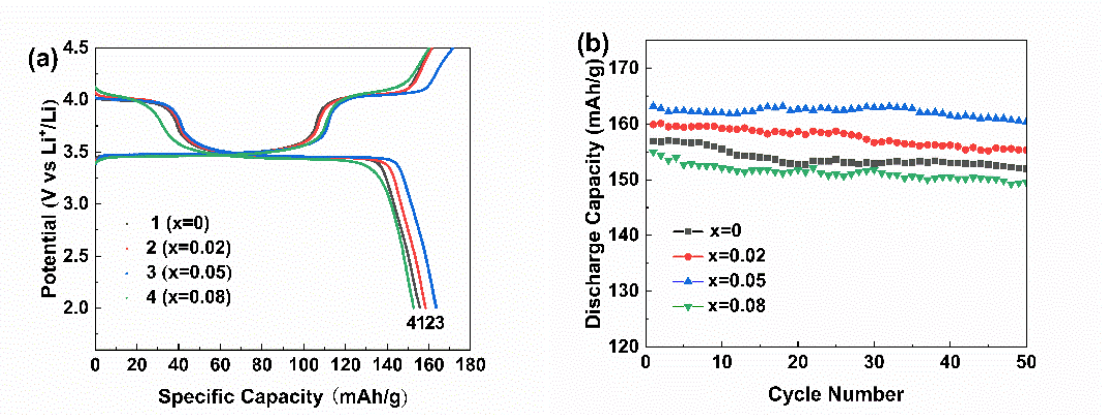

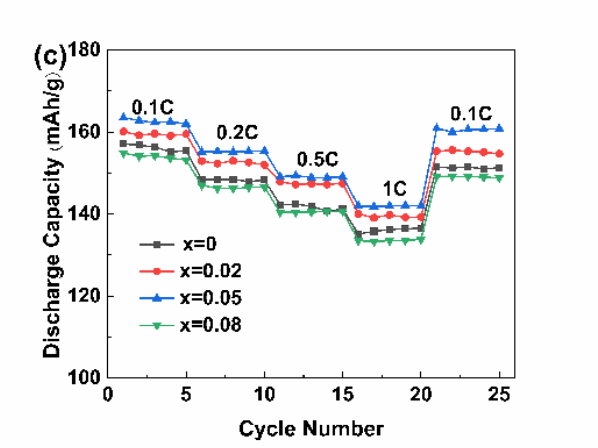

Figure 5. Electrochemical performances of the $LiFe_{0.7}Mn_{0.3-x}Mg_xPO_4/C$ samples: (a) first charge/discharge curves at 0.1C, (b) cycle performances at 0.1C, and (c) rate performances.

Table 3 Comparison of the electrochemical performances of materials prepared in other studies and the $LiFe_{0.7}Mn_{0.25}Mg_{0.05}PO_4/C$ material prepared in this study

Material	C-Rate	Capacity ($mAhg^{-1}$)	Reference
$LiFe_{0.8}Mn_{0.2}PO_4/C$	0.1C	150.0 mAh/g	[24]
$LiFe_{0.4}Mn_{0.6-x}Cr_xPO_4/C$	0.1C	163.7 mAh/g	[27]
$LiFe_{0.48}Mn_{0.48}Mg_{0.04}PO_4$	0.1C	146.3 mAh/g	[41]
$Li_{0.98}Na_{0.02}(Fe_{0.65}Mn_{0.35})_{0.97}Mg_{0.03}PO_4/C$	0.1C	147.7 mAh/g	[42]
$LiFe_{0.7}Mn_{0.25}Mg_{0.05}PO_4/C$	0.1C	163.2 mAh/g	This work

To further investigate the reasons for the improved electrochemical properties of the material, cyclic voltammetry (CV) and electrochemical impedance (EIS) tests were also carried out on the samples. Fig. 6 shows the cyclic voltammetry curves of the $LiFe_{0.7}Mn_{0.3-x}Mg_xPO_4/C$ samples at a sweep rate of 0.1 mV/s in the voltage range of 2.0–4.5 V. Both the Mg^{2+}-doped and undoped samples had two pairs of sharp and symmetric redox peaks corresponding to the Fe^{2+}/Fe^{3+} and Mn^{2+}/Mn^{3+} redox electrode potentials, which indicated that all samples exhibited good electrochemical reversibility. The intensities of the redox peaks of Fe^{3+}/Fe^{2+} and Mn^{3+}/Mn^{2+} increased gradually when the Mg^{2+} doping amount increased from 0% to 5% but decreased significantly again when the doping amount reached 8%. Furthermore, when the Mg doping amount was 0%, the redox potential differences were 0.189 and 0.143 V for Fe^{2+}/Fe^{3+} and Mn^{2+}/Mn^{3+}, respectively. The potential difference between the two pairs of redox peaks gradually decreased as the Mg doping amount started to increase, with the smallest potential differences of 0.154 and 0.088 V at 5% Mg doping. The differences increased to 0.295 and 0.148 V when the doping amount was increased to 8%, and it was found that the polarization was the smallest at 5% Mg^{2+} doping and had better reversibility than the other samples. This indicated that the appropriate amount of Mg^{2+} doping could effectively improve the reversibility of the lithium-ion reaction and reduce the lattice volume change due to Li^+ de-embedding, thereby reducing the lattice distortion and lowering

the diffusion resistance. This ultimately increased the electronic conductivity and effectively improved the electrochemical properties of the material.

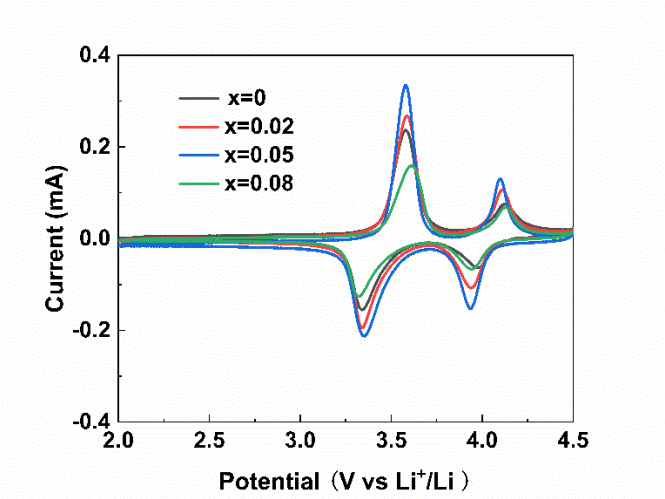

Figure 6. Cyclic voltametric curves of $LiFe_{0.7}Mn_{0.3-x}Mg_xPO_4/C$.

To investigate the reaction kinetics process of the material, electrochemical impedance tests were performed on four samples. Fig. 7(a) shows the Nyquist plots of the AC impedance spectra of the samples with different Mg^{2+} doping amounts and their equivalent circuit diagrams. It can be seen that the Nyquist plot consisted of high-frequency semicircles and low-frequency diagonal lines corresponding to the charge transfer resistance (Rct) and Warburg impedance (Wo), respectively, and the intercept of the high-frequency semicircle with the Z' axis corresponded to the ohmic impedance (Rs) [43, 44].

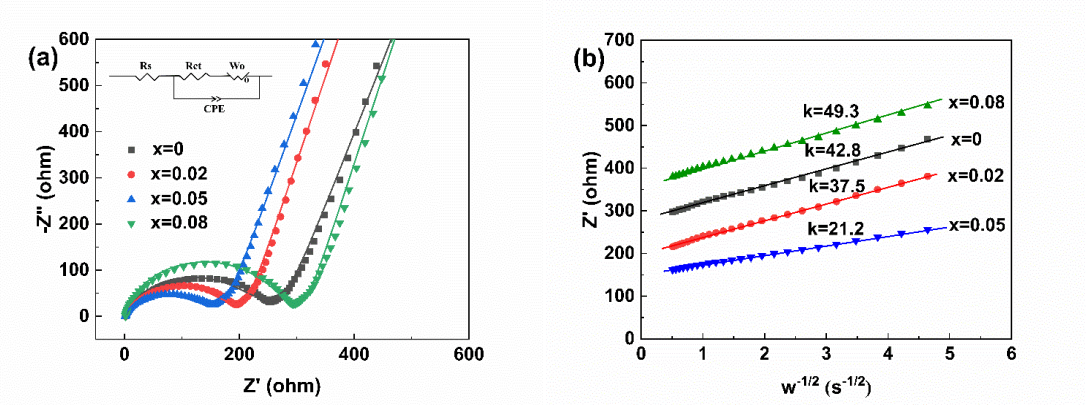

Figure 7. (a) Nyquist plot and equivalent circuit diagram for $LiFe_{0.7}Mn_{0.3-x}Mg_xPO_4/C$ material and (b) linear relationship between the inverse square root of the angular frequency and the Warburg impedance.

The high-frequency semicircle was related to the charge transfer resistance at the interface of the active material, while the low-frequency slope represented the Warburg impedance caused by the diffusion of lithium ions in the electrode. Fig. 7(a) shows that the intercepts of the high-frequency parts

of the semicircles and the Z' axes of the four samples almost coincided, indicating that their Rs values were basically the same. In addition, with the increase in the Mg doping, the Rct values of the four samples were 215.2, 194.0, 175.6, and 264.1 Ω, respectively, among which $LiFe_{0.7}Mn_{0.25}Mg_{0.05}PO_4/C$ had the smallest charge transfer impedance. This indicated that the appropriate amount of Mg^{2+} doping improved the interfacial transfer rate of Li^+ during the electrochemical diffusion kinetics and effectively improved the material. The electronic conductivity of the material was effectively improved.

To further confirm that the lithium-ion diffusion process was enhanced, the lithium-ion diffusion coefficient (D_{Li}) was calculated using the parameters obtained by fitting the impedance curve. The diagonal straight line in the low-frequency region of the EIS corresponded to the diffusion of lithium ions in the cathode material. The lithium-ion diffusion coefficient (D_{Li}) was calculated using the following equation based on the parameters in the low-frequency sloping straight line section [45, 46]:

$$Z_{re} = R_{ct} + R_s + \sigma\omega^{-\frac{1}{2}}, \quad (1)$$

$$D_{Li} = \frac{R^2T^2}{2S^2n^4F^4{C_{Li}}^2\sigma^2}, \quad (2)$$

where R is the ideal gas constant, T is the absolute temperature, S is the electrode contact area, n is the number of electrons transferred by the electrochemical reaction, F is the Faraday constant, C is the concentration of Li+ in the $LiFe_{0.7}Mn_{0.3-x}Mg_xPO_4/C$, and σ is the Warburg factor [47].

According to equation (1), Z' and $\omega^{-1/2}$ are linearly related. From the plot of Z and $\omega^{-1/2}$ shown in Fig. 4(b), it can be seen that they were highly linearly related. From this plot, we obtained the Warburg factors σ from the slopes of the curves for the different samples. It can be calculated that $LiFe_{0.7}Mn_{0.3-x}Mg_xPO_4/C$ (x = 0, 0.02, 0.05, and 0.08) had lithium-ion diffusion coefficients of 2.91×10^{-14}, 3.80×10^{-14}, 1.19×10^{-13}, and 2.19×10^{-14}, respectively. It is easy to see by comparison that $LiFe_{0.7}Mn_{0.25}Mg_{0.05}PO_4/C$ had the largest lithium-ion diffusion coefficient, which was 4.1 times higher than that of the undoped Mg^{2+} sample. This result indicated that Mg^{2+} doping into the lattice not only improved the electrical conductivity of the material but also significantly increased the lithium-ion diffusion coefficient of the material. It can therefore be concluded that the improved electrochemical properties of the $LiFe_{0.7}Mn_{0.25}Mg_{0.05}PO_4/C$ samples were the joint result of the improvement of both the conductivity and the lithium-ion diffusion coefficient.

4. CONCLUSION

In this paper, $LiFe_{0.7}Mn_{0.3-x}Mg_xPO_4/C$ (x = 0, 0.02, 0.05, and 0.08) materials were successfully prepared by a high-temperature solid-phase method, and a series of characterization results showed that all the samples had olivine structures, indicating that the small amount of Mg^{2+} doping did not change the structure of the material itself. SEM and EDS analyses showed that all the samples had uniform particle sizes and uniform distributions of the various elements, and carbon was uniformly encapsulated on the surfaces of the materials. A small amount of Mg^{2+} doping could effectively improve the electrochemical properties of the material, but too much Mg^{2+} doping could deteriorate the electrochemical properties of the material. $LiFe_{0.7}Mn_{0.25}Mg_{0.05}PO_4/C$ achieved a specific discharge capacity of 163.2 mAh/g at 0.1C, with a retention rate of 98.6% after 50 cycles. In addition, the specific discharge capacity could reach 142.0 mAh/g even at 1C, which was 83.5% of the theoretical capacity,

demonstrating the excellent multiplicative performance and cycling stability of the material. Cyclic voltammetry and AC impedance studies have revealed that Mg^{2+} doping can significantly reduce the polarization of the material, increase the electrical conductivity and lithium-ion diffusion rate, and ultimately effectively improve the electrochemical properties of the material.

DISCLOSURE STATEMENT
No potential conflict of interest was reported by the authors.

FUNDING
This work is supported by Hubei Provincial Major Technology Innovation project of China [No.2018AAA056], The International Science & Technology Cooperation Program of China [2016YFE0124300].

References

1. J. Li, M. Xiang, Y. Wang, J. Wu, H. Zhao, H. Liu, *J. Mater. Chem. A*, 5 (2017) 7952-7960.
2. B. Zhang, H. Wei, J. Zhang, G. Ji, J. Zhang, X. Ou, *Ceram. Int.*, 45 (2019) 13607-13613.
3. S. Yaroslavtsev, S. Novikova, V. Rusakov, N. Vostrov, T. Kulova, A. Skundin, A. Yaroslavtsev, *Solid State Ionics*, 317 (2018) 149-155.
4. X. Liu, T. Feng, X. Wang, X. Li, *Rare Metal Mat. Eng.*, 45 (2016) 207-211.
5. J. Sun, Z. Li, X. Ren, L. Wang, G. Liang, *J. Alloys Compd.*, 773 (2019) 788-795.
6. C.L. Fan, C.R. Lin, S.C. Han, J. Chen, L.F. Li, Y.m. Bai, K.H. Zhang, X. Zhang, *New J. Chem.*, 38 (2014) 795-801.
7. H. Lee, S. Kim, N.S. Parmar, J.H. Song, K.y. Chung, K.B. Kim, J.W. Choi, *J. Power Sources*, 434 (2019)
8. J. Lu, W. Li, C. Shen, D. Tang, L. Dai, G. Diao, M. Chen, *Ionics*, 25 (2019) 4075-4082.
9. Y. Zhang, J.A. Alarco, J.Y. Nerkar, A.S. Best, G.A. Snook, P.C. Talbot, *Mater. Charact.*, 162 (2020)
10. F. Wen, H.B. Shu, Y.Y. Zhang, J.J. Wan, W.H. Huang, X.K. Yang, R.Z. Yu, L. Liu, X.Y. Wang, *Electrochim. Acta*, 214 (2016) 85-93.
11. V. Ragupathi, P. Panigrahi, G.S. Nagarajan, *Appl. Surf. Sci.*, 495 (2019)
12. F. Wen, T.A. Lv, P. Gao, B. Wu, Q. Liang, Y. Zhang, H. Shu, X. Yang, L. Liu, X. Wang, *Electrochim. Acta*, 276 (2018) 134-141.
13. Z. Xiao, Y. He, X. Li, L. Zhang, Z. Ding, *Chemistryselect*, 3 (2018) 4222-4227.
14. J. Li, S.H. Luo, Q. Wang, S. Yan, J. Feng, H. Liu, X. Ding, P. He, *Electrochim. Acta*, 289 (2018) 415-421.
15. L. Yang, W. Deng, W. Xu, Y. Tian, A. Wang, B. Wang, G. Zou, H. Hou, W. Deng, X. Ji, *J. Mater. Chem. A*, 9 (2021) 14214-14232.
16. L. Dou, E. Han, L. Li, L. Zhu, S. Qiao, H. Liu, *Ionics*, 25 (2019) 2487-2499.
17. H. Yang, C. Fu, Y. Sun, L. Wang, T. Liu, *Carbon*, 158 (2020) 102-109.
18. X. Fu, Z. Chang, K. Chang, B. Li, H. Tang, E. Shangguan, X.Z. Yuan, H. Wang, *Electrochim. Acta*, 178 (2015) 420-428.
19. J. Zhang, S.H. Luo, Q.X. Ren, D.J. Zhang, Y. Qin, *Appl. Surf. Sci.*, 530 (2020)
20. H. Zhuang, Y. Bao, Y. Nie, Y. Qian, Y. Deng, G. Chen, *Electrochim. Acta*, 314 (2019) 102-114.
21. S. Dhaybi, B. Marsan, *J. Alloys Compd.*, 766 (2018) 1067-1073.
22. B.C. Sin, S.U. Lee, B.S. Jin, H.S. Kim, J.S. Kim, S.I. Lee, J. Noh, Y. Lee, *Solid State Ionics*, 260 (2014) 2-7.

23. G. Zhang, E. Han, L. Zhu, Q. Jing, *Ionics*, 21 (2015) 319-324.
24. A.F. Liu, Z.B. Wen, Y.F. Liu, Z.H. Hu, *Funct. Mater. Lett.*, 4 (2011) 319-322.
25. W. Huang, J. Hu, L. Yang, W. Zhao, Z. Wang, H. Wang, Z. Guo, Y. Li, J. Liu, K. Yang, F. Pan, *Acs. Appl. Mater. Inter.*, 11 (2019) 957-962.
26. P. Gao, Z. Tan, F.Q. Cheng, H.H. Zhou, S.T. Tan, *Acta. Phys-Chim Sin.*, 28 (2012) 338-342.
27. P. Xiao, Y. Cai, X. Chen, Z. Sheng, C. Chang, *Rsc Adv.*, 7 (2017) 31558-31566.
28. S. Okada, S. Sawa, M. Egashira, J.i. Yamaki, M. Tabuchi, H. Kageyama, T. Konishi, A. Yoshino, *J. Power Sources*, 97 (2001) 430-432.
29. H. Liu, J. Xie, *J. Mater. Process. Tech.*, 209 (2009) 477-481.
30. Z. Yang, J. Xia, L. Zhi, W. Zhang, B. Pei, *Ionics*, 20 (2014) 169-174.
31. S.Y. Chung, J.T. Bloking, Y.M. Chiang, *Nature Mater.*, 1 (2002) 123-128.
32. Y.K. Sun, S.M. Oh, H.K. Park, B. Scrosati, *J. Adv. Mater.*, 23 (2011) 5050-5054.
33. S.M. Oh, S.T. Myung, Y.S. Choi, K.H. Oh, Y.K. Sun, *J. Mater. Chem. A*, 21 (2011) 19368-19374.
34. M.S. Kim, J.P. Jegal, K.C. Roh, K.B. Kim, *J. Mater. Chem. A*, 2 (2014) 10607-10613.
35. L. Wu, S.K. Zhong, J.Q. Liu, F. Lv, K. Wan, *Mater. Lett.*, 89 (2012) 32-35.
36. K. Kisu, E. Iwama, W. Onishi, S. Nakashima, W. Naoi, K. Naoi, *J. Mater. Chem. A*, 2 (2014) 20789-20798.
37. W. Xiang, Y. Zhong, Y. Tang, H. Shen, E. Wang, H. Liu, B. Zhong, X. Guo, *J. Alloys Compd.*, 635 (2015) 180-187.
38. N.N. Bramnik, K.G. Bramnik, K. Nikolowski, M. Hinterstein, C. Baehtz, H. Ehrenberg, *Electrochem. Solid-State Lett.*, 8 (2005) A379.
39. S. Li, X. Meng, Q. Yi, J. Antonio Alonso, M.T. Fernandez-Diaz, C. Sun, Z.L. Wang, *Nano Energy*, 52 (2018) 510-516.
40. D. Jang, K. Palanisamy, J. Yoon, Y. Kim, W.S. Yoon, *J. Power Sources*, 244 (2013) 581-585.
41. D. Jang, K. Palanisamy, Y. Kim, W.S. Yoon, *J. Electrochem. Sci. Te.*, 4 (2013) 102-107.
42. S. Qiao, L. Zhu, E. Han, L. Li, C. Du, Y. He, *Int. J. Electrochem. Sci.*, 14 (2019) 11616-11629.
43. A.Y. Shenouda, H.K. Liu, *J. Power Sources*, 185 (2008) 1386-1391.
44. B. Li, C. Han, Y.-B. He, C. Yang, H. Du, Q.H. Yang, F. Kang, *Energ. Environ. Sci.*, 5 (2012) 9595-9602.
45. M.J. Lee, M. Noh, M.H. Park, M. Jo, H. Kim, H. Nam, J. Cho, *J. Mater. Chem. A*, 3 (2015) 13453-13460.
46. J. Li, Q. Qu, L. Zhang, L. Zhang, H. Zheng, *J. Alloys Compd.*, 579 (2013) 377-383.
47. L. Dou, E. Han, L. Li, L. Zhu, S. Qiao, H. Liu, *Ionics*, 25 (2019) 2487-2499.